

# Simulated Multispectral Temperature and Atmospheric Composition Retrievals for the JPL GEO-IR Sounder

Vijay Natraj<sup>1</sup>, Ming Luo<sup>1</sup>, Jean-Francois Blavier<sup>1</sup>, Vivienne H. Payne<sup>1</sup>, Derek J. Posselt<sup>1</sup>, Stanley P. Sander<sup>1</sup>, Zhao-Cheng Zeng<sup>2,3</sup>, Jessica L. Neu<sup>1</sup>, Denis Tremblay<sup>4</sup>, Longtao Wu<sup>1</sup>, Jacola A. Roman<sup>1</sup>, Yen-Hung Wu<sup>1</sup>, Leonard I. Dorsky<sup>1</sup>

<sup>1</sup>Jet Propulsion Laboratory, California Institute of Technology, Pasadena, CA 91109, USA

<sup>2</sup>Joint Institute for Regional Earth System Science and Engineering, University of California, Los Angeles, CA 90095, USA

<sup>3</sup>Division of Geological and Planetary Sciences, California Institute of Technology, Pasadena, CA 91125, USA

<sup>4</sup>Global Science Technology, USA

*Correspondence to:* Vijay Natraj ([vijay.natraj@jpl.nasa.gov](mailto:vijay.natraj@jpl.nasa.gov))

**Abstract.** Satellite measurements enable quantification of atmospheric temperature, humidity, wind fields, and trace gas vertical profiles. The majority of current instruments operate on polar orbiting satellites and either in the thermal/mid-wave or in the shortwave infrared spectral regions. We present a new multispectral instrument concept for improved measurements from geostationary orbit (GEO) with sensitivity to the boundary layer. The JPL GEO-IR sounder, which is an imaging Fourier Transform Spectrometer, uses a wide spectral range (1–15.4  $\mu\text{m}$ ), encompassing both reflected solar and thermal emission bands to improve sensitivity to the lower troposphere and boundary layer. We perform retrieval simulations for both clean and polluted scenarios that also encompass different temperature and humidity profiles. The results illustrate the benefits of combining shortwave and thermal infrared measurements. In particular, the former adds information in the boundary layer, while the latter helps to separate near-surface and mid-tropospheric variability. The performance of the JPL GEO-IR sounder is similar to or better than currently operational instruments. The proposed concept is expected to improve weather forecasting, severe storm tracking and forecasting, and also benefit local and global air quality and climate research.

 © Author(s) 2021. This work is distributed under the Creative Commons Attribution 4.0 License.

33 **1 Introduction**

34 The Program of Record (PoR) of current and planned satellite observations, as described in the 2017  
35 US Earth Science Decadal Survey (*NASEM*, 2018), includes a range of spectrally-resolved radiance  
36 measurements in the thermal and shortwave infrared (TIR and SWIR) wavelength regions that provide  
37 key information on atmospheric temperature (TATM), water vapor ( $H_2O$ ) and a range of trace gases (see  
38 Table 1 for a definition of spectral range designations). The TIR region can be further subdivided into  
39 midwave, longwave and very longwave infrared (MIR, LWIR and VLWIR) regions. Profiling of key  
40 gases including CO,  $CH_4$ , and  $CO_2$  with sensitivity to planetary boundary layer (PBL) abundances was  
41 identified as a gap in current capability in the 2017 Decadal Survey, as was the promise of multispectral  
42 approaches for addressing this gap. In fact, combining radiances from the (thermal emission dominated)  
43 TIR and (solar reflection dominated) SWIR spectral regions has been shown to increase the vertical  
44 information content for these gases, providing improved information on near-surface variations relative  
45 to retrievals from the thermal alone (e.g., *Christi and Stephens*, 2004; *Worden et al.*, 2010; *Kuai et al.*,  
46 2013; *Worden et al.*, 2015; *Fu et al.*, 2016; *Zhang et al.*, 2018; *Schneider et al.*, 2021). Such retrievals  
47 have the potential to extend the utility of satellite products for air quality forecasting, greenhouse gas  
48 monitoring and carbon cycle research. In addition, combining TIR and SWIR infrared radiances also  
49 offers opportunities for increasing the vertical information of  $H_2O$  retrievals in the PBL, another topic  
50 highlighted by the Decadal Survey and by the NASA Decadal Survey PBL Incubation Study Team  
51 (*Teixeira et al.*, 2021). Under clear-sky conditions, the SWIR provides sensitivity to  $H_2O$  (e.g., *Noël et*  
52 *al.*, 2005; *Trent et al.*, 2018; *Nelson et al.*, 2016), CO (e.g., *Buchwitz et al.*, 2004; *Deeter et al.*, 2009;  
53 *Landgraf et al.*, 2016; *Borsdorff et al.*, 2017; 2018),  $CH_4$  (e.g., *Buchwitz et al.*, 2005; *Frankenberg et al.*,  
54 2006; *Yokota et al.*, 2009; *Hu et al.*, 2018; *Parker et al.*, 2020) and  $CO_2$  (e.g., *Buchwitz et al.*, 2005;  
55 *Yokota et al.*, 2009; *O'Dell et al.*, 2018) throughout the full atmospheric column, providing  
56 complementary information to the TIR radiances that are strongly sensitive to the details of the profile  
57 of TATM,  $H_2O$  and trace gases but have variable sensitivity to the PBL, depending on surface and  
58 atmospheric conditions.

59 Table 2 shows a list of current and planned missions making spectrally-resolved, spaceborne TIR  
60 and SWIR measurements. In Low Earth Orbit (LEO), the MOPITT instrument on the Terra platform has  
61 been providing a record of TIR+SWIR CO for over two decades (*Buchholz et al.*, 2021). GOSAT and  
62 GOSAT-2 provide spectrally-resolved TIR and SWIR radiances on the same platform, with coverage of  
63 SWIR  $CO_2$  and  $CH_4$  bands, as well as  $H_2O$  absorption (*Trent et al.*, 2018), but not SWIR CO. The  
64 TROPOMI instrument on the Sentinel-5P satellite flies in formation with the CrIS instrument on the  
65 **Suomi**-NPP satellite, providing near-coincident observations of TIR and SWIR, presenting opportunities

66 for multispectral retrievals of CO and CH<sub>4</sub>. Measurements from geostationary (GEO) orbit can provide  
67 contiguous horizontal (~4 km) and temporal (full sounding disk coverage in 1–2 hours) resolution not  
68 possible from LEO (e.g., *Schmit et al.*, 2009). The IRS instrument onboard the Meteosat Third  
69 Generation Sounder platform will track the four-dimensional structure of TATM and H<sub>2</sub>O (*Holmlund et*  
70 *al.*, 2021). The GIIRS instrument on the Fengyun-4 meteorological satellite has similar capabilities (*Yang*  
71 *et al.*, 2017). *Adkins et al.* (2021) describe in comprehensive detail the value of a hyperspectral IR  
72 sounder in GEO orbit. Based on this report, an advanced high-resolution IR sounder has been  
73 recommended for the Geostationary Extended Observations (GeoXO) mission  
74 (<https://www.nesdis.noaa.gov/next-generation-satellites/geostationary-extended-observations-geoxo>).  
75 However, none of the current/planned instruments/missions listed in Table 2 provide TIR + SWIR  
76 measurements from GEO on the same platform.

77 Here, we describe an instrument concept, called the JPL GEO-IR Sounder, that would provide  
78 profiling of TATM, H<sub>2</sub>O, CO, CH<sub>4</sub> and CO<sub>2</sub>, as well as numerous other species important for air quality  
79 and the hydrological cycle, from a geostationary platform. The JPL GEO-IR Sounder is an imaging  
80 Fourier transform spectrometer that utilizes high-speed digital focal plane arrays to record simultaneous  
81 TIR and SWIR spectra from each pixel of the array (640 × 480 or 1024 × 1024 format). The primary  
82 advantages of this sounder include the following:

- 83 • Coincident spatial and temporal retrievals of trace gases and TATM using both SWIR and TIR bands  
84 multiple times per day
- 85 • Combined TIR and SWIR retrievals provide for enhanced vertical resolution with PBL visibility for  
86 TATM, humidity and multiple trace gases
- 87 • Capability for retrievals of 4-D winds from combinations of TATM and H<sub>2</sub>O temporal imagery as  
88 recently described using GIIRS data (*Ma et al.*, 2021; *Yin et al.*, 2021)
- 89 • Providing data products that are not readily obtained by combining retrievals from PoR LEO and  
90 GEO sounders.

91 This paper is organized as follows: in Section 2, we describe the scenarios used in the simulations.  
92 Section 3 provides brief descriptions of the radiative transfer (RT), instrument and inverse models. We  
93 discuss the considerations imposed on simulated JPL GEO-IR Sounder retrievals in Section 4. In Section  
94 5, we present results for TATM, H<sub>2</sub>O and trace gas retrievals from simulated GEO-IR Sounder  
95 measurements for both individual spectral regions and combinations. The relevance of these simulated  
96 retrievals for Observation System Simulation Experiments is discussed in Section 6. We arrive at some  
97 preliminary conclusions in Section 7. In particular, we show that the JPL GEO-IR Sounder would, for  
98 the first time, enable high spatial and temporal resolution simultaneous retrievals in the TIR and SWIR,

99 which together provide more vertical profile information and improved sensitivity to the PBL than either  
100 spectral region alone.

101

102 **2 Scenarios**

103 Representative atmospheric conditions, including TATM, H<sub>2</sub>O and pollutant distributions, surface  
104 temperature and other interferents are needed to understand satellite instrument performance. Using  
105 Weather Research and Forecasting model coupled to Chemistry (WRF-Chem) simulations at 4 km spatial  
106 resolution over the continental United States (Mary Barth, personal communication), we examined about  
107 200 atmospheric profiles at six local times for two days in July 2006 over 17 locations that represent a  
108 range of diurnal meteorological conditions and a variety of air quality scenarios. For the purposes of  
109 these simulations, we assume clear-sky conditions. Simulation of conditions with significant aerosol  
110 loading and cloud interference adds significant complexity and is beyond the scope of this study. We  
111 calculate molecular absorption coefficients using the Line-By-Line Radiative Transfer Model  
112 (LBLRTM; *Clough et al.*, 2005).

113 The main goal of these simulations is to evaluate the retrieval characteristics of TATM, H<sub>2</sub>O, and  
114 trace gases for different instrument configurations. From our database of over 200 summer-time  
115 atmospheric profiles over the continental US, we selected two representative daytime atmospheres; one  
116 near Houston to support the weather-focused **Observation System Simulation Experiment** (OSSE)  
117 analyses and the background trace gas case, and another in West Virginia that has more enhanced trace  
118 gas pollutants near the surface. Note that we kept the solar and viewing geometry as well as the surface  
119 albedo constant in order to isolate the effects of different boundary layer trace gas concentrations. Figure  
120 1 shows the profile plots for TATM, H<sub>2</sub>O, and trace gases that we examine in this manuscript (O<sub>3</sub>, CO,  
121 CH<sub>4</sub> and CO<sub>2</sub>) at the two locations.

122 The emissivity is obtained from a database structured by month and latitude/longitude coordinates. To  
123 populate the database, we used a global land use and land cover classification system developed by the  
124 U.S. Geological Survey (*Anderson et al.*, 1976) and mapped them into spectra from the ECOSTRESS  
125 spectral library (*Baldridge et al.*, 2009; *Meerdink et al.*, 2019; <http://speclib.jpl.nasa.gov/>), as described  
126 in the TES Algorithm Theoretical Basis Document (*Beer et al.*, 2002). The albedo is calculated from the  
127 emissivity using Kirchoff's law.

128 The location and times of the WRF-Chem profiles were used to calculate the solar viewing geometry,  
129 assuming a geostationary satellite at 95 W. The NOAA solar position calculator was used to verify the  
130 solar zenith and solar azimuth calculations (<http://www.srrb.noaa.gov/highlights/sunrise/azel.html>).

131

132 **3 Models**

133 **3.1 Radiative transfer model**

134 We use the accurate and numerically efficient two-stream-exact-single-scattering (2S-ESS) RT  
135 model (*Spurr and Natraj*, 2011; *Xi et al.*, 2015). This forward model is different from a typical two-  
136 stream model in that the two-stream approximation is used only to calculate the contribution of multiple  
137 scattering to the radiation field. Single scattering is treated in a numerically exact manner using all  
138 moments of the scattering phase function. High computational efficiency is achieved by employing the  
139 two-stream approximation for multiple scattering calculations. The exact single scattering calculation  
140 largely eliminates biases due to the severe truncation of the phase function inherent in a traditional two-  
141 stream approximation. Therefore, the 2S-ESS model is much more accurate than a typical two-stream  
142 model, and produces radiances and Jacobians that are typically within a few percent of numerically exact  
143 calculations and in most cases with biases much less than a percent. This model has been widely used  
144 for the remote sensing of greenhouse gases and aerosols (*Xi et al.*, 2015; *Zhang et al.*, 2015, 2016; *Zeng*  
145 *et al.*, 2017, 2018). Aerosols are not included in the analysis since the main objective was to investigate  
146 the impact of combining multiple spectral bands and of varying instrument parameters. However, the RT  
147 model has the capability of handling generic aerosol types.

148 The 2S-ESS RT model is used to generate monochromatic radiances at the top of the atmosphere  
149 for the atmospheric profiles and surface conditions near Houston over the entire spectral range considered  
150 for the JPL GEO-IR Sounder. Figure 2 shows the spectral radiance computed on a  $0.002 \text{ cm}^{-1}$  wavelength  
151 grid. We also calculate the individual contributions of each absorbing gas to the radiance. The gaseous  
152 absorption features have different spectral distributions and line strengths, which can be used to identify  
153 spectral windows for profile retrievals and recognize interfering gases that also absorb strongly in the  
154 same channels.

155 **3.2 Instrument model**

156 This section starts with a brief description of the spectrometer, primarily to define the terms used in  
157 the instrument model. We then detail the focal plane arrays and the optical filter that determine the  
158 bandpasses of the instrument. The processing steps of the instrument model are then explained. Finally,  
159 we show some of the resulting spectra produced by the model.

160 *3.2.1 Optics Overview*

161 The JPL GEO IR Sounder uses a Michelson interferometer, which modulates the light that passes  
162 through it. The interferometer is characterized by two main parameters: the spectral resolution, which is  
163 directly proportional to the maximum optical path difference (MOPD) between the two arms of the  
164 interferometer, and the optical throughput or étendue, which is given by the product of the area of the

165 aperture stop and the angular field of view ( $A\Omega$ ). From geostationary orbit, a ground pixel of 2.1 km  
166 subtends an angle of 58.7  $\mu$ rad and for a Focal Plane Array (FPA) of 1024×1024 pixels, the overall FOV  
167 is 60 mrad; this fits well within the Fourier Transform Spectrometer (FTS) design parameters. In parallel  
168 with the light from the target scene, a beam from an internal metrology laser travels through the  
169 interferometer. This laser is used to precisely measure the optical path difference, to within a small  
170 fraction of the laser wavelength. An imaging FTS (IFTS) shares many of the principles of the traditional  
171 FTS, the main difference is that the detector is replaced with an FPA. The main challenge in the IFTS  
172 design is in the FPA, which must operate at high frame rate (0.5–1 kHz) and at high dynamic range (14–  
173 16 bits) to properly digitize the interferograms.

174 *3.2.2 Focal Plane Arrays*

175 The JPL GEO-IR Sounder FPA optics uses a dichroic to split the interferometer output along the  
176 wavelength dimension: radiation from 1  $\mu$ m to 5.3  $\mu$ m is sent towards FPA #1 and radiation from 5.3  $\mu$ m  
177 to 15.4  $\mu$ m is directed to FPA #2. Whereas FPA #2 is a single-color detector, handling its full domain at  
178 all times, FPA #1 is a dual-color detector. The two colors of FPA #1 are operated sequentially: recording  
179 either the 1  $\mu$ m to 3  $\mu$ m domain (SWIR; FPA #1a) or the 3  $\mu$ m to 5.3  $\mu$ m domain (MWIR; FPA #1b).  
180 This dual-color operation is implemented inside the FPA by having two distinct detectors in an optical  
181 "sandwich". It is designed to minimize the effect of photon noise in the low-light MWIR and SWIR  
182 domains. Furthermore, the SWIR FPA #1a bandpass is narrowed by a triple-band optical filter, tailored  
183 to the regions that contain absorption bands of interest (Figure 3). As listed in Table 3, the SWIR domains  
184 of interest are: (1) 4210–4350  $\text{cm}^{-1}$ , (2) 4810–4900  $\text{cm}^{-1}$ , (3) 6000–6150  $\text{cm}^{-1}$  and (4) 6170–6290  $\text{cm}^{-1}$ .  
185 Based on previous optical filter studies, we allow 200  $\text{cm}^{-1}$  for the filter slope on either side. Since the  
186 gap between the first two domains would therefore be small, and the signal there is low, these have been  
187 merged (4210–4900  $\text{cm}^{-1}$ ). Domains (3) and (4) have also been combined (6000–6290  $\text{cm}^{-1}$ ). In addition,  
188 the 1.27  $\mu$ m oxygen band (7780–8010  $\text{cm}^{-1}$ ) will be used to measure the light path. We believe that it is  
189 best to specify the 50% transmission points for the filter bands, as that is where the slope is maximum  
190 and hence most easily verified. With a 200  $\text{cm}^{-1}$  transition region, the 50% point will be 100  $\text{cm}^{-1}$  outside  
191 of the bandpasses. Hence the final triple-band filter configuration is: 4110–5000  $\text{cm}^{-1}$  (2.000–2.433  $\mu$ m),  
192 5900–6390  $\text{cm}^{-1}$  (1.565–1.695  $\mu$ m), 7680–8110  $\text{cm}^{-1}$  (1.233–1.302  $\mu$ m). The triple-band filter physically  
193 covers the two-color FPA #1. It is intended to limit the photon flux only in the SWIR mode of operation,  
194 with the detector that is sensitive over the 1–3  $\mu$ m domain (FPA #1a). The filter must also be transparent  
195 over the 3–5.3  $\mu$ m domain of the other shared detector (FPA #1b). It may be possible to combine the  
196 first band of the triple-band filter (2–2.433  $\mu$ m) with this MWIR transparency need (3–5.3  $\mu$ m) but this  
197 has not been simulated in this study.

198     3.2.3 *Instrument Model Description*

199     The Instrument Model for the JPL GEO IR Sounder allows us to explore the instrument trade space  
200     and its effect on retrieved atmospheric composition. It includes the ability to convolve synthetic spectra  
201     and Jacobians with the instrument line shape (ILS). The model performs the following steps:

202     1. Reads synthetic data from the radiative transfer model. The radiance spectrum is extended using  
203     blackbody curves simulating the Earth and the Sun, and converted to a photon flux spectrum. After this  
204     step, the spectrum is in units of photons/m<sup>2</sup>/sr/cm<sup>-1</sup>/s.

205     2. Convolves the spectrum with the theoretical FTS ILS, given as:  $2Lsinc(2\sigma L)$ , where L is the MOPD  
206     and  $sinc(x)=\sin(\pi x)/\pi x$ . This expression of the ILS has unit area, and hence the convolution does not  
207     change the overall magnitude or the units of the spectrum. It does, however, reduce the spectral resolution,  
208     broadening all sharp features. In the same step, we resample the spectrum on a coarser grid, i.e., we  
209     “decimate” the spectrum. For example, in the current simulations, we reduce the wavenumber interval  
210     by a factor of 50, from 0.002 cm<sup>-1</sup> to 0.1 cm<sup>-1</sup>.

211     3. Scales the spectrum by the étendue of the instrument. After this step, the units of the spectrum are  
212     photons/cm<sup>-1</sup>/s.

213     4. Applies further scaling to account for the single output design (where half the light is sent through the  
214     instrument and the other half sent back to the source), losses in the metallic coatings and at the uncoated  
215     optical interfaces (i.e., compensator and back side of beamsplitter), the efficiency of the beamsplitter  
216     coating, the quantum efficiency of the detector, and the integration time of the analog-to-digital converter.  
217     After this step, the units of the spectrum are photoelectrons/cm<sup>-1</sup>.

218     5. Applies bandpass limits caused either by an optical filter or the working domain of the detector.

219     6. Applies the Fourier transform to convert the spectrum into an interferogram.

220     7. Computes the number of photoelectrons counted in each interferogram data sample. From this, we can  
221     compute the photon noise. Subsequently, white noise is added to the interferogram with a root mean  
222     square amplitude matching the computed photon noise.

223     8. Simulates the interferogram digitization, performed for each pixel within the Read Out Integrated  
224     Circuit of the two FPAs.

225     9. Produces the final spectrum by Fourier transform. The signal to noise ratio (SNR) is then evaluated  
226     by computing the noise level in blacked-out regions on either side of the instrument bandpass, and by  
227     locating the maximum signal within the bandpass.

228     3.2.4 *Spectral Results*

229     Figure 3 shows a JPL GEO-IR Sounder model spectrum for FPA #1a, covering the SWIR domain.  
230     Figure 4 shows a similar spectrum for the VLWIR, LWIR and MWIR FPA bands: FPA #2 covers the

231 VLWIR and LWIR domains, and FPA #1b covers the MWIR domain. The spectral ranges include the  
232 range utilized by existing TIR sounders (AIRS, CrIS, IASI) and selected bands in the SWIR. In particular,  
233 the FPA #2 spectral range contains critical information for radiance assimilation by weather forecasting  
234 algorithms (see, e.g., *Eresmaa et al.*, 2017). The spectral resolution (MOPD) of the JPL GEO-IR Sounder  
235 is configurable. For these simulations, we choose to look at three possible MOPD options: a CrIS-like  
236 spectral resolution (0.8 cm MOPD,  $0.625 \text{ cm}^{-1}$  resolution, described as nominal spectral resolution or  
237 NSR in Table 4), an intermediate option (2 cm MOPD,  $0.25 \text{ cm}^{-1}$  resolution), and a high spectral  
238 resolution option (5 cm MOPD,  $0.1 \text{ cm}^{-1}$  resolution, described as full spectral resolution or FSR in Table  
239 4). In order to make for an "apples to apples" comparison, we consider the same integration time (1  
240 millisecond per interferogram point) for these three options. The integration time is driven by the high  
241 spectral resolution option. The native and binned (footprint-averaged) ground sampling distance (GSD)  
242 are also indicated in Table 4.

### 243 3.3 Inverse model

244 We use an optimal estimation approach (*Rodgers*, 2000) and perform linear retrievals from  
245 simulated radiances described in the previous section. The spectral differences of the modeled and the  
246 satellite measured radiances and the differences of the species profile and the *a priori* profile are  
247 mathematically minimized, weighted by the measurement error and the *a priori* constraint. The species  
248 profile can then be derived optimally.

249 The *a priori* constraint vectors for TATM and H<sub>2</sub>O are obtained from forecast fields from the NASA  
250 Global Modeling and Assimilation Office, supplied for use within the TES retrieval algorithm (*Bowman*  
251 *et al.*, 2006). *A priori* constraint matrices are constructed, using the method described in *Kulawik et al.*  
252 (2006), from an altitude-dependent combination of zeroth, first and second order derivatives of the  
253 profiles. For TATM and H<sub>2</sub>O, the square roots of the diagonals of the respective constraint matrices are  
254 on the order of 1.8–2.2 K and 15–18%, respectively. *A priori* vectors for O<sub>3</sub>, CO and CH<sub>4</sub> are taken from  
255 calculations using the Model for OZone And Related chemical Tracers (MOZART3) (*Brasseur et al.*,  
256 1998; *Park et al.*, 2004) that were performed for the purpose of construction of trace gas climatologies  
257 for the Aura mission. For O<sub>3</sub>, the square root of the diagonal of the constraint matrix is on the order of  
258 25% in the troposphere, 40% in the stratosphere and 15% above. For CO, this is set to 30% over the  
259 entire atmosphere, while for CH<sub>4</sub>, the values range from 2–10%. The constraint matrices for CO are the  
260 same as those used by the MOPITT algorithm (*Deeter et al.*, 2010). For CO<sub>2</sub>, the *a priori* vector and  
261 constraint used are described in *Kulawik et al.* (2010). The square root of the diagonal of the constraint  
262 matrix ranges from 1.2–2%. We note that these profile constraints were developed for TIR instruments,  
263 and may therefore not capture strong near-surface variability. There could be scope for increasing the

264 near-surface information content via development of updated constraints, although that work is outside  
265 of the scope of this study.

266 The end-to-end retrieval analysis provides averaging kernels, which describe the sensitivity of the  
267 retrieved atmospheric state to the true state; degrees of freedom for signal (DOFS), which denote the  
268 pieces of vertical information contained in the retrieved profile; and retrieval errors. These metrics are  
269 used for evaluating the retrieval results for a variety of spectral bands, and spectral and spatial resolutions.  
270

#### 271 **4 Considerations for simulated retrievals**

272 For the retrieval simulations described here, we consider a somewhat idealized scenario.  
273 Simulations have been performed for clear-sky, no-aerosol conditions. In retrievals from actual measured  
274 radiances, even for a clear-sky, non-scattering atmosphere, there is always some forward model error  
275 due to, e.g., uncertainties in spectroscopy, interfering species and the treatment of the surface. With real  
276 data, these kinds of uncertainties can lead to significant systematic errors in the retrievals, particularly  
277 for well-mixed greenhouse gases such as CH<sub>4</sub> and CO<sub>2</sub>. For the simulations presented here, we have  
278 considered only the error term associated with measurement noise.

279 The measurement noise associated with the simulated radiance is obtained using the instrument  
280 model described in Section 3.2. The JPL GEO-IR sounder concept is configurable in terms of spectral  
281 range and spectral resolution, with a native spatial resolution that corresponds to a 2.1 km footprint on  
282 the ground. Different configurations of the instrument concept will affect the number of photons  
283 available in each channel and therefore impact the signal to noise. For a given integration time, lower  
284 spectral resolution leads to correspondingly higher SNR. The SNR of the observed radiance spectra can  
285 be increased by increasing the integration time. For geostationary observations, this leads to a trade-off  
286 between measurement noise and temporal resolution. An increase of the throughput (etendue) leads to  
287 lower noise (Schwantes *et al.*, 2002).

288 In retrievals from real data, higher spectral resolution can offer advantages in terms of ability to  
289 distinguish between the target molecule and interfering spectral signatures from other molecules with  
290 features in the spectral range of interest, despite the increase in measurement noise. In the results  
291 presented in this study, that advantage in reduction of systematic error is not accounted for. The SNR  
292 can also be increased by aggregating spatially. For example, aggregating four 2.1 km footprints would  
293 increase the SNR by a factor of two. Depending on the application of the measurements, there may be  
294 some advantage to trading spatial resolution for a gain in SNR.

#### 295 **5 Results**

297 **5.1 TATM and H<sub>2</sub>O retrievals**

298 High spectral resolution is necessary to provide the vertically resolved TATM and H<sub>2</sub>O information  
299 critical for numerical weather prediction and for many other applications including local extreme weather  
300 conditions and global climate change. Current satellite-based TATM and H<sub>2</sub>O retrievals mainly utilize  
301 TIR spectral measurements. Here we also examine information gained from adding SWIR measurements.  
302 Tables 5 and 6 list the possible choices of frequency range for TATM and H<sub>2</sub>O retrievals. Some of these  
303 spectral ranges are used in current operational missions, while some are candidates for future missions.  
304 We compare results for three values of spectral resolution and for two values of spatial resolution.

305 Examining the above DOFS tables, we see competing effects of spectral resolution (MOPD) and  
306 measurement noise. As described in Section 3.2, the measurement noise (Noise Equivalent Spectral  
307 Radiance, NESR) is estimated for a fixed integration time for both the 2.1 and 4.2 km ground sampling  
308 distance (GSD) configurations. The NESR for the MOPD = 0.8 cm instrument is therefore smaller than  
309 that for the MOPD = 2 or 5 cm instruments. Typically, however, the higher spectral resolution  
310 instruments provide larger DOFS than the NSR instrument. For H<sub>2</sub>O retrievals, the optimal DOFS are  
311 provided by the intermediate resolution instrument.

312 The differences in DOFS for the two GSD values are obvious. This shows the trade-off between  
313 spatial resolution and retrieval vertical resolution and precision (not listed). Both GSDs provide high  
314 precision, high vertical resolution TATM and H<sub>2</sub>O retrievals. We estimate the tropospheric vertical  
315 resolution for TATM to be 1.5–2 km with <0.5 K precision, and for H<sub>2</sub>O to be 1–2 km with ~5%  
316 precision. In comparison, representative tropospheric values for AIRS are 1 km for TATM and 2 km for  
317 H<sub>2</sub>O (*Irion et al.*, 2018).

318 The selection of spectral regions also affects the TATM and H<sub>2</sub>O products. For example, using the  
319 VLWIR+LWIR+MWIR domain provides much more sensitivity compared to using MWIR alone. Figure  
320 5 shows averaging kernel plots for TATM and H<sub>2</sub>O for the 4.2 km GSD option for four spectral band  
321 combinations: VLWIR+LWIR, MWIR, SWIR, and VLWIR+LWIR+MWIR+SWIR. The characteristics  
322 of the TIR TATM and H<sub>2</sub>O retrievals are very similar to those obtained by currently operating  
323 instruments. We note that the sensitivity of SWIR retrievals is mostly near the surface. Further, the  
324 measurement noise in the SWIR was reduced by a factor of 5 in these figures by averaging 25 pixels,  
325 thereby reducing the effective GSD to 21 km. Note that this is worse than the 15 km AIRS/CrIS native  
326 resolution but better than the 45 km that the TATM and H<sub>2</sub>O products are typically reported on. **Further,**  
327 **while 5×5 pixels may be required for trace gas retrievals in the SWIR (see section 5.2) and is therefore**  
328 **a little worse than AIRS/CrIS, we measure TIR and SWIR at the same time, eliminating bias from**  
329 **observing with separate instruments.**

330 **5.2 Trace gas retrievals**

331 Among many possible detectable trace gases from the extended spectral radiance measurements, we  
332 selected to examine profile retrieval characteristics for O<sub>3</sub>, CO, CH<sub>4</sub> and CO<sub>2</sub> for the given instrument  
333 configurations (see Table 3 for retrieval spectral ranges). Table 7 lists DOFS for the chosen trace gases  
334 for the West Virginia scenario. Results for the FSR option are largely similar to those for the intermediate  
335 spectral resolution instrument and are hence not shown. The DOFS in Table 7 are broadly consistent  
336 with previously published work on species profile retrievals from satellite observations (Beer, 2006;  
337 Connor *et al.*, 2008; Deeter *et al.*, 2009, 2015; George *et al.*, 2009; Kulawik *et al.*, 2010; Worden *et al.*,  
338 2010, 2013; Clerbaux *et al.*, 2015; Fu *et al.*, 2016; Smith and Barnet, 2020). For a given spectral  
339 resolution instrument, the higher DOFS in retrievals for the larger GSD case for all species are due to  
340 the reduced measurement noise. For a given GSD, the DOFS are slightly higher for the NSR case  
341 compared to the MOPD = 2 cm case, but the differences are small. It is worth reiterating that these  
342 simulated retrievals represent an idealized scenario, where we assume perfect knowledge of interfering  
343 species in the spectral range for any given target species. In this scenario, with a constant integration  
344 time, the NSR option provides similar results to the MOPD = 2 cm option due to the trade-off between  
345 spectral resolution and instrument noise.

346 Figure 6 shows averaging kernel plots for CO for MWIR- and SWIR-only scenarios and for  
347 combined MWIR+SWIR retrievals. The combination of wavelength regions provides improved  
348 sensitivity to the lower troposphere compared to either spectral region alone. CO<sub>2</sub> retrievals (Figure 7)  
349 benefit the most from the combination of VLWIR+MWIR+SWIR retrievals. The SWIR domain adds  
350 sensitivity in the lower troposphere and near the surface. The characteristics of the CO<sub>2</sub> retrievals are in  
351 good agreement with OCO-2/3 observations. For CH<sub>4</sub> (Figure 8), the addition of SWIR bands also  
352 provides noticeable enhancement in lower tropospheric and near-surface sensitivity. For CO retrievals,  
353 the contribution of the SWIR to the near-surface sensitivity is less pronounced. The stronger contribution  
354 of SWIR measurements to the total DOFS for CH<sub>4</sub> and CO<sub>2</sub> compared to CO is a result of three factors:  
355 (1) lower top of the atmosphere solar irradiance in the CO spectral region relative to the CH<sub>4</sub> and CO<sub>2</sub>  
356 regions, (2) lower surface albedo, and (3) larger absorption, primarily by H<sub>2</sub>O and CH<sub>4</sub>. Our results for  
357 O<sub>3</sub> are broadly consistent with published results for LWIR satellite observations (e.g., Nassar *et al.*, 2008;  
358 Smith and Barnet, 2020). Figures 6–8 use the same effective GSD of 21 km in the SWIR as described in  
359 Section 5.1.

360

361 **6 Discussion: Use of GEO-IR Information in Data Assimilation and Observation System**  
362 **Simulation Experiments**

363 We have focused in this paper on the characteristics of the measurements and retrievals that we  
364 expect to obtain from the GEO-IR observing platform. While this paper does not deal directly with the  
365 use of this information in a data assimilation system, the results we have presented lay the necessary  
366 groundwork for future work in this area. In particular, the detailed characterization of uncertainties in the  
367 TATM and H<sub>2</sub>O retrievals provided by this study can be directly incorporated into a set of weather  
368 forecast OSSEs. We have begun this research, and will report on the results in a subsequent paper. Note  
369 that, for a weather forecast OSSE to be credible, it is crucial to represent the synthetic measurements as  
370 accurately as possible. TATM and H<sub>2</sub>O precision and total error are reported in Table 8; it can be seen  
371 that the errors for the MWIR-only configuration are on the order of the errors in CrIS and AIRS retrievals,  
372 while the full-spectrum JPL GEO-IR Sounder configuration yields total errors that are smaller than those  
373 from either CrIS or AIRS. As such, assimilation of information from JPL GEO-IR Sounder  
374 measurements is expected *a priori* to have as much or greater impact on weather forecasts compared  
375 with existing hyperspectral sounders. Note that the total error in the full-spectral-range TATM and H<sub>2</sub>O  
376 retrievals is equivalent to, or less than, the uncertainty reported for radiosonde measurements of these  
377 quantities (Rienecker *et al.*, 2008; Table 3.5.2).

378 We also note that there will be particular advantages and challenges in assimilating the high  
379 temporal resolution data that will be available from the JPL GEO-IR Sounder. The clear advantage is the  
380 ability to observe rapidly evolving processes (e.g., the environment around thunderstorms and hurricanes;  
381 see, e.g., Li *et al.*, 2018). This information is not available from the current LEO constellation. However,  
382 many modern data assimilation systems are configured for assimilation of intermittent data (at best  
383 hourly in operational data assimilation systems). While four-dimensional variational data assimilation  
384 (4D-Var) is capable of ingesting data at non-synoptic times, assimilation of sub-hourly data remains  
385 challenging. It is likely that all but the most rapid-update data assimilation systems will require  
386 modification to make best use of the high time frequency geostationary soundings provided by the JPL  
387 GEO-IR Sounder.

388

## 389 7 Conclusions

390 In this paper, we present an end-to-end retrieval study for a proposed FTS instrument covering the  
391 entire infrared spectral range from 1–15  $\mu\text{m}$  from a geostationary satellite orbit. An instrument model is  
392 used to derive realistic measurement radiance and noise for several diurnal observations over small  
393 ground footprints (e.g., 2.1 km). We perform TATM and trace gas profile retrievals for the JPL GEO-IR  
394 Sounder that covers the entire VLWIR, LWIR, MWIR and SWIR spectral domains. Retrieval  
395 characteristics, such as DOFS and measurement error, are examined in order to evaluate the performance

396 of several instrument configurations. These configurations include VLWIR-, LWIR-, MWIR-, and  
397 SWIR-only and their combinations, and different spectral and spatial resolutions, for a realistic  
398 geostationary observing system making field-of-view observations at fixed time intervals. Two summer-  
399 time atmospheres are used: a scenario near Houston as a clean-air case, and one in West Virginia  
400 representing a polluted scenario. We analyze TATM, H<sub>2</sub>O, O<sub>3</sub>, CO, CH<sub>4</sub> and CO<sub>2</sub> profile retrievals.

401 High spectral resolution can provide improved ability to distinguish absorption lines of the target  
402 species from interferents. In the case of species (such as O<sub>3</sub>) where much of the total column lies in the  
403 stratosphere, higher spectral resolution also provides enhanced ability to separate the tropospheric signal  
404 from the stratospheric signal. When the total integration time is fixed, there is a trade-off between spectral  
405 resolution and noise. In the idealized retrievals presented here, we assume perfect knowledge of  
406 interfering species. In this case, three different MOPDs provide comparable results in terms of DOFS.  
407 However, in the real world, we would expect higher spectral resolution to offer advantages in terms of  
408 reduction in systematic errors.

409 Compared to single spectral region instruments, e.g., only LWIR or MWIR, combinations of  
410 VLWIR/LWIR/MWIR/SWIR enhance the sensitivity of the retrievals to the lower troposphere. In our  
411 analyses, we find that the contributions from the SWIR in the combined measurements are noticeable for  
412 both trace gas and TATM retrievals, especially when the ground pixels are averaged to reduce  
413 measurement noise in the SWIR. In particular, the SWIR measurements add information in the lower  
414 troposphere and for near-surface species retrievals.

415 We limit the spatial resolution choices to GSD = 2.1 km and 4.2 km in our simulations. Especially  
416 for multi-band retrievals, the results are realistically adequate for many research applications for both  
417 ground sampling footprints. We compare performance metrics (e.g., NESR and SNR) for the proposed  
418 instrument with values for several current/past satellite instruments in multiple spectral bands. The  
419 performance of the JPL GEO-IR Sounder is similar to or better than currently operational instruments.  
420 At the same time, the JPL GEO-IR Sounder provides much higher spatial and temporal resolution and a  
421 wider range of trace gases than current instruments that combine TIR and SWIR. The derived retrieval  
422 characteristics (e.g., DOFS and retrieval errors) also compare favorably with currently available  
423 products.

424

## 425 **Data availability**

426 The code and data are available from the authors upon request.

## 427 **Author contributions**

428 SPS, Y-HW and LID conceived the work. VN provided the radiative transfer model, led the  
429 simulated retrieval work, and prepared the manuscript. ML, J-FB and ZZ assisted with the retrievals. ML  
430 provided the trace gas absorption and inverse models. JLN provided the profiles for the simulations. SSK  
431 provided the emissivity database and advised on the retrieval constraints. J-FB provided the instrument  
432 model. VHP and SPS helped analyze the simulation results. LW, JAR and DJP provided the connection  
433 with OSSEs. All listed authors contributed to the review and editing of this manuscript.

434

#### 435 **Competing interests**

436 The authors declare that they have no conflict of interest.

437

#### 438 **Acknowledgements**

439 A portion of this research was carried out at the Jet Propulsion Laboratory, California Institute of  
440 Technology, under a contract with the National Aeronautics and Space Administration  
441 (80NM0018D0004). The authors acknowledge S. Kulawik for helpful discussions on retrieval  
442 constraints.

443

#### 444 **Financial Support**

445 The authors acknowledge support from the National Oceanic and Atmospheric Administration  
446 through BAA-NOAA-GEO-2019, and the Jet Propulsion Laboratory Advanced Concepts Program.

447 **References**

448

449 Adkins, J., Alsheimer, F., Ardanuy, P., Boukabara, S., Casey, S., Coakley, M., Conran, J., Cucurull, L.,  
450 Daniels, J., Ditchek, S. D., Gallagher, F., Garrett, K., Gerth, J., Goldberg, M., Goodman, S., Grigsby, E.,  
451 Griffin, M., Griffin, V., Hardesty, M., Iturbide, F., Kalluri, S., Knuteson, R., Krimchansky, A., Lauer,  
452 C., Lindsey, D., McCarty, W., McCorkel, J., Ostroy, J., Pogorzala, D., Revercomb, H., Rivera, R.,  
453 Seybold, M., Schmit, T., Smith, B., Sullivan, P., Talaat, E., Tewey, K., Todirita, M., Tremblay, D.,  
454 Vassiliadis, D., Weir, P., and Yoe, J.: Geostationary Extended Observations (GeoXO) hyperspectral  
455 infrared sounder value assessment report, NOAA Tech. Rep., National Environmental Satellite, Data,  
456 and Information Service, <https://doi.org/10.25923/7zvz-fv26>, 2021.

457

458 Anderson, J. R., Hardy, E. E., Roach, J. T., and Witmer, R. E.: A land use and land cover classification  
459 system for use with remote sensor data, USGS Tech Rep., <https://doi.org/10.3133/pp964>, 1976.

460

461 Baldridge, A. M., S. J. Hook, C. I. Grove, and G. Rivera: The ASTER spectral library version 2.0,  
462 *Remote Sens. Environ.*, 113(4), 711–715, <https://doi.org/10.1016/j.rse.2008.11.007>, 2009.

463

464 Beer, R., Bowman, K. W., Brown, P. D., Clough, S. A., Eldering, A., Goldman, A., Jacob, D. J., Lampel,  
465 M., Logan, J. A., Luo, M., Murcray, F. J., Osterman, G. B., Rider, D. M., Rinsland, C. P., Rodgers, C.  
466 D., Sander, S. P., Shepard, M., Sund, S., Ustinov, E., Worden, H. M., and Worden, J.: Tropospheric  
467 Emission Spectrometer (TES) level 2 algorithm theoretical basis document, Version 1.15, JPL D-16474,  
468 Jet Propulsion Laboratory, Pasadena, California (available at <https://eospso.gsfc.nasa.gov/atbd-category/53>), 2002.

470

471 Beer, R.: TES on the Aura mission: Scientific objectives, measurements, and analysis overview, *IEEE*  
472 *Trans. Geosci. Remote Sens.*, 44(5), 1102–1105, <https://doi.org/10.1109/TGRS.2005.863716>, 2006.

473

474 Bowman, K. W., Rodgers, C. D., Kulawik, S. S., Worden, J., Sarkissian, E., Osterman, G., Steck, T.,  
475 Luo, M., Eldering, A., Shepard, M., Worden, H., Lampel, M., Clough, S., Brown, P., Rinsland, C.,  
476 Gunson, M., and Beer, R.: Tropospheric Emission Spectrometer: Retrieval method and error analysis,  
477 *IEEE Trans. Geosci. Remote Sens.*, 44(5), 1297–1307, <https://doi.org/10.1109/TGRS.2006.871234>,  
478 2006.

479

480 Borsdorff, T., Aan de Brugh, J., Hu, H., Aben, I., Hasekamp, O., and Landgraf, J.: Measuring carbon  
481 monoxide with TROPOMI: First results and a comparison with ECMWF-IFS analysis data, *Geophys.*  
482 *Res. Lett.*, 45(6), 2826–2832, <https://doi.org/10.1002/2018GL077045>, 2018.

483

484 Borsdorff, T., aan de Brugh, J., Hu, H., Nédélec, P., Aben, I., and Landgraf, J.: Carbon monoxide column  
485 retrieval for clear-sky and cloudy atmospheres: A full-mission data set from SCIAMACHY 2.3  $\mu\text{m}$   
486 reflectance measurements, *Atmos. Meas. Tech.*, 10(5), 1769–1782, <https://doi.org/10.5194/amt-10-1769-2017>, 2017.

488

489 Brasseur, G. P., Hauglustaine, D. A., Walters, S., Rasch, P. J., Muller, J. F., Granier, C., and Tie, X. X.:  
490 MOZART, a global chemical transport model for ozone and related chemical tracers 1. Model  
491 description, *J. Geophys. Res.*, 103(D21), 28265–28289, <https://doi.org/10.1029/98JD02397>, 1998.

492

493 Buchholz, R. R., Worden, H. M., Park, M., Francis, G., Deeter, M. N., Edwards, D. P., Emmons, L. K.,  
494 Gaubert, B., Gille, J., Martinez-Alonso, S., Tang, W., Kumar, R., Drummond, J. R., Clerbaux, C.,  
495 George, M., Coheur, P.-F., Hurtmans, D., Bowman, K. W., Luo, M., Payne, V. H., Worden, J. R., Chin,  
496 M., Levy, R. C., Warner, J., Wei, Z., and Kulawik, S. S.: Air pollution trends measured from Terra: CO  
497 and AOD over industrial, fire-prone, and background regions, *Remote Sens. Environ.*, 256, 112275,  
498 <https://doi.org/10.1016/j.rse.2020.112275>, 2021.

499

500 Buchwitz, M., de Beek, R., Bramstedt, K., Noël, S., Bovensmann, H., and Burrows, J. P.: Global carbon  
501 monoxide as retrieved from SCIAMACHY by WFM-DOAS, *Atmos. Chem. Phys.*, 4(7), 1945–1960,  
502 <https://doi.org/10.5194/acp-4-1945-2004>, 2004.

503

504 Buchwitz, M., de Beek, R., Noël, S., Burrows, J. P., Bovensmann, H., Bremer, H., Bergamaschi, P.,  
505 Körner, S., and Heimann, M.: Carbon monoxide, methane and carbon dioxide columns retrieved from  
506 SCIAMACHY by WFM-DOAS: Year 2003 initial data set, *Atmos. Chem. Phys.*, 5(12), 3313–3329,  
507 <https://doi.org/10.5194/acp-5-3313-2005>, 2005.

508

509 Christi, M. J., and Stephens, G. L.: Retrieving profiles of atmospheric CO<sub>2</sub> in clear sky and in the  
510 presence of thin cloud using spectroscopy from the near and thermal infrared: A preliminary case study,  
511 *J. Geophys. Res.*, 109(D4), D04316, <https://doi.org/10.1029/2003jd004058>, 2004.

512 Clough, S. A., Shephard, M. W., Mlawer, E., Delamere, J. S., Iacono, M., Cady-Pereira, K., Boukabara,  
513 S., and Brown, P. D.: Atmospheric radiative transfer modeling: a summary of the AER codes, *J. Quant.*  
514 *Spectrosc. Radiat. Transfer*, 91(2), 233–244, <https://doi.org/10.1016/j.jqsrt.2004.05.058>, 2005.

515

516 Connor, B. J., Boesch, H., Toon, G., Sen, B., Miller, C., and Crisp, D.: Orbiting Carbon Observatory:  
517 Inverse method and prospective error analysis, *J. Geophys. Res.*, 113, D05305,  
518 <https://doi.org/10.1029/2006JD008336>, 2008.

519

520 Clerbaux, C., Hadji-Lazaro, J., Turquety, S., George, M., Boynard, A., Pommier, M., Safieddine, S.,  
521 Coheur, P.-F., Hurtmans, D., Clarisse, L., and Van Damme, M.: Tracking pollutants from space: Eight  
522 years of IASI satellite observation, *C. R. Géosci.*, 347(3), 134–144,  
523 <https://doi.org/10.1016/j.crte.2015.06.001>, 2015.

524

525 Deeter, M. N., Edwards, D. P., Gille, J. C., and Drummond, J. R.: CO retrievals based on MOPITT near-  
526 infrared observations, *J. Geophys. Res.*, 114(D4), D04303, <https://doi.org/10.1029/2008JD010872>, 2009.

527

528 Deeter, M. N., Edwards, D. P., Gille, J. C., Emmons, L. K., Francis, G., Ho, S.-P., Mao, D., Masters, D.,  
529 Worden, H. M., Drummond, J. R., and Novelli, P. C.: The MOPITT version 4 CO product: Algorithm  
530 enhancements, validation, and long-term stability, *J. Geophys. Res.*, 115(D7), D07306,  
531 <https://doi.org/10.1029/2009JD013005>, 2010.

532

533 Deeter, M. N., Edwards, D. P., Gille, J. C., and Worden, H. M.: Information content of MOPITT CO  
534 profile retrievals: Temporal and geographical variability, *J. Geophys. Res.*, 120(24), 12723–12738,  
535 <https://doi.org/10.1002/2015JD024024>, 2015.

536

537 Eresmaa, R., Letertre-Danczak, J., Lupu, C., Bormann, N., and McNally, A. P.: The assimilation of  
538 Cross-track Infrared Sounder radiances at ECMWF, *Q. J. R. Meteorolog. Soc.*, 143(709), 3177–3188,  
539 2017, <https://doi.org/10.1002/qj.3171>.

540

541 Frankenberg, C., Meirink, J. F., Bergamaschi, P., Goede, A. P. H., Heimann, M., Körner, S., Platt, U.,  
542 van Weele, M., and Wagner, T.: Satellite chartography of atmospheric methane from SCIAMACHY on  
543 board ENVISAT: Analysis of the years 2003 and 2004, *J. Geophys. Res.*, 111(D7), D07303,  
544 <https://doi.org/10.1029/2005JD006235>, 2006.

545 Fu, D., Bowman, K. W., Worden, H. M., Natraj, V., Worden, J. R., Yu, S., Veefkind, P., Aben, I.,  
546 Landgraf, J., Strow, L., and Han, Y.: High-resolution tropospheric carbon monoxide profiles retrieved  
547 from CrIS and TROPOMI, *Atmos. Meas. Tech.*, 9(6), 2567–2579, doi:10.5194/amt-9-2567-2016, 2016.

548

549 George, M., Clerbaux, C., Hurtmans, D., Turquety, S., Coheur, P.-F., Pommier, M., Hadji-Lazaro, J.,  
550 Edwards, D. P., Worden, H., Luo, M., Rinsland, C., and McMillan, W.: Carbon monoxide distributions  
551 from the IASI/METOP mission: Evaluation with other space-borne remote sensors, *Atmos. Chem. Phys.*,  
552 9(21), 8317–8330, <https://doi.org/10.5194/acp-9-8317-2009>, 2009.

553

554 Holmlund, K., Grandell, J., Schmetz, J., Stuhlmann, R., Bojkov, B., Munro, R., Lekouara, M., Coppens,  
555 D., Viticchie, B., August, T., Theodore, B., Watts, P., Dobber, M., Fowler, G., Bojinski, S., Schmid, A.,  
556 Salonen, K., Tjemkes, S., Aminou, D., and Blythe, P.: Meteosat Third Generation (MTG): Continuation  
557 and innovation of observations from geostationary orbit, *Bull. Am. Meteorol. Soc.*, 102(5), E990–E1015,  
558 <https://doi.org/10.1175/BAMS-D-19-0304.1>, 2021.

559

560 Hu, H., Landgraf, J., Detmers, R., Borsdorff, T., Aan de Brugh, J., Aben, I., Butz, A., and Hasekamp,  
561 O.: Toward global mapping of methane with TROPOMI: First results and intersatellite comparison to  
562 GOSAT, *Geophys. Res. Lett.*, 45(8), 3682–3689, <https://doi.org/10.1002/2018GL077259>, 2018.

563

564 Irion, F. W., Kahn, B. H., Schreier, M. M., Fetzer, E. J., Fishbein, E., Fu, D., Kalmus, P., Wilson, R. C.,  
565 Wong, S., and Yue, Q.: Single-footprint retrievals of temperature, water vapor and cloud properties from  
566 AIRS, *Atmos. Meas. Tech.*, 11(2), 971–995, <https://doi.org/10.5194/amt-11-971-2018>, 2018.

567

568 Kuai, L., Worden, J., Kulawik, S., Bowman, K., Lee, M., Biraud, S. C., Abshire, J. B., Wofsy, S. C.,  
569 Natraj, V., Frankenberg, C., Wunch, D., Connor, B., Miller, C., Roehl, C., Shia, R.-L., and Yung, Y.:  
570 Profiling tropospheric CO<sub>2</sub> using Aura TES and TCCON instruments, *Atmos. Meas. Tech.*, 6(1), 63–79,  
571 <https://doi.org/10.5194/amt-6-63-2013>, 2013.

572

573 Kulawik, S. S., Osterman, G., Jones, D.B.A., and Bowman, K.W.: Calculation of altitude-dependent  
574 Tikhonov constraints for TES nadir retrievals, *IEEE Trans. Geosci. Remote Sens.*, 44(5), 1334–1342,  
575 <https://doi.org/10.1109/TGRS.2006.871206>, 2006.

576

577 Kulawik, S. S., Jones, D. B. A., Nassar, R., Irion, F. W., Worden, J. R., Bowman, K. W., Machida, T.,  
578 Matsueda, H., Sawa, Y., Biraud, S. C., Fischer, M. L., and Jacobson, A. R.: Characterization of  
579 Tropospheric Emission Spectrometer (TES) CO<sub>2</sub> for carbon cycle science, *Atmos. Chem. Phys.*, 10(12),  
580 5601–5623, <https://doi.org/10.5194/acp-10-5601-2010>, 2010.

581

582 Landgraf, J., Aan de Brugh, J., Scheepmaker, R., Borsdorff, T., Hu, H., Houweling, S., Butz, A., Aben,  
583 I., and Hasekamp, O.: Carbon monoxide total column retrievals from TROPOMI shortwave infrared  
584 measurements, *Atmos. Meas. Tech.*, 9(10), 4955–4975, <https://doi.org/10.5194/amt-9-4955-2016>, 2016.

585

586 Li, Z., Li, J., Wang, P., Lim, A., Li, J., Schmit, T. J., Atlas, R., Boukabara, S.-A., and Hoffman, R. N.:  
587 **Value-added impact of geostationary hyperspectral infrared sounders on local severe storm forecasts—**  
588 **via a quick regional OSSE**, *Adv. Atmos. Sci.*, 35(10), 1217–1230, <https://doi.org/10.1007/s00376-018-8036-3>, 2018.

589

590

591 Ma, Z., Li, J., Han, W., Li, Z., Zeng, Q., Menzel, W. P., Schmit, T. J., Di, D., and Liu, C.-Y.: Four-  
592 dimensional wind fields from geostationary hyperspectral infrared sounder radiance measurements with  
593 high temporal resolution, *Geophys. Res. Lett.*, 48(14), e2021GL093794,  
594 <https://doi.org/10.1029/2021GL093794>, 2021.

595

596 Meerdink, S. K., Hook, S. J., Roberts, D. A., and Abbott, E. A.: The ECOSTRESS spectral library version  
597 1.0, *Remote Sens. Environ.*, 230(111196), 1–8, <https://doi.org/10.1016/j.rse.2019.05.015>, 2019.

598

599 Nassar, R., Logan, J. A., Worden, H. M., Megretskaya, I. A., Bowman, K. W., Osterman, G. B.,  
600 Thompson, A. M., Tarasick, D. W., Austin, S., Claude, H., Dubey, M. K., Hocking, W. K., Johnson, B.  
601 J., Joseph, E., Merrill, J., Morris, G. A., Newchurch, M., Oltmans, S. J., Posny, F., Schmidlin, F. J.,  
602 Vomel, H., Whiteman, D. N., and Witte, J. C.: Validation of Tropospheric Emission Spectrometer (TES)  
603 nadir ozone profiles using ozonesonde measurements, *J. Geophys. Res.*, 113(D15), D15S17,  
604 <https://doi.org/10.1029/2007JD008819>, 2008.

605

606 National Academies of Sciences, Engineering, and Medicine (NASEM): *Thriving on Our Changing*  
607 *Planet: A Decadal Strategy for Earth Observation from Space*, The National Academies Press,  
608 Washington, DC, <https://doi.org/10.17226/24938>, 2018.

609

610 Nelson, R. R., Crisp, D., Ott, L. E., and O'Dell, C. W.: High-accuracy measurements of total column  
611 water vapor from the Orbiting Carbon Observatory-2, *Geophys. Res. Lett.*, 43(23), 12261–12269,  
612 <https://doi.org/10.1002/2016GL071200>, 2016.

613

614 Noël, S., Buchwitz, M., Bovensmann, H., and Burrows, J. P.: Validation of SCIAMACHY AMC-DOAS  
615 water vapour columns, *Atmos. Chem. Phys.*, 5(7), 1835–1841, <https://doi.org/10.5194/acp-5-1835-2005>,  
616 2005.

617

618 O'Dell, C. W., Eldering, A., Wennberg, P. O., Crisp, D., Gunson, M. R., Fisher, B., Frankenberg, C.,  
619 Kiel, M., Lindqvist, H., Mandrake, L., Merrelli, A., Natraj, V., Nelson, R. R., Osterman, G. B., Payne,  
620 V. H., Taylor, T. R., Wunch, D., Drouin, B. J., Oyafuso, F., Chang, A., McDuffie, J., Smyth, M., Baker,  
621 D. F., Basu, S., Chevallier, F., Crowell, S. M. R., Feng, L., Palmer, P. I., Dubey, M., García, O. E.,  
622 Griffith, D. W. T., Hase, F., Iraci, L. T., Kivi, R., Morino, I., Notholt, J., Ohyama, H., Petri, C., Roehl,  
623 C. M., Sha, M. K., Strong, K., Sussmann, R., Te, Y., Uchino, O., and Velazco, V. A.: Improved retrievals  
624 of carbon dioxide from the Orbiting Carbon Observatory-2 with the version 8 ACOS algorithm, *Atmos.*  
625 *Meas. Tech.*, 11(12), 6539–6576, <https://doi.org/10.5194/amt-2018-257>, 2018.

626

627 Park, M., Randel, W. J., Kinnison, D. E., Garcia, R. R., and Choi, W.: Seasonal variation of methane,  
628 water vapor, and nitrogen oxides near the tropopause: Satellite observations and model simulations, *J.*  
629 *Geophys. Res.*, 109(D3), <https://doi.org/10.1029/2003JD003706>, 2004.

630

631 Parker, R. J., Webb, A., Boesch, H., Somkuti, P., Barrio Guillo, R., Di Noia, A., Kalaitzi, N., Anand, J.  
632 S., Bergamaschi, P., Chevallier, F., Palmer, P. I., Feng, L., Deutscher, N. M., Feist, D. G., Griffith, D.  
633 W. T., Hase, F., Kivi, R., Morino, I., Notholt, J., Oh, Y.-S., Ohyama, H., Petri, C., Pollard, D. F., Roehl,  
634 C., Sha, M. K., Shiomi, K., Strong, K., Sussmann, R., Té, Y., Velazco, V. A., Warneke, T., Wennberg,  
635 P. O., and Wunch, D.: A decade of GOSAT proxy satellite CH<sub>4</sub> observations, *Earth Syst. Sci. Data*, 12(4),  
636 3383–3412, <https://doi.org/10.5194/essd-12-3383-2020>, 2020.

637

638 Rienecker, M. M., Suarez, M. J., Todling, R., Bacmeister, J., Takacs, L., Liu, H.-C., Gu, W., Sienkiewicz,  
639 M., Koster, R. D., Gelaro, R., Stajner, I., and Nielsen, J. E.: The GEOS-5 Data Assimilation System—  
640 Documentation of Versions 5.0.1, 5.1.0, and 5.2.0, *NASA Tech. Rep. NASA/TM-2008-104606*, 27, 2008.

641

642 Rodgers, C. D.: Inverse Methods for Atmospheric Sounding: Theory and Practice, World Scientific,  
643 Singapore, 2000.

644

645 Schmit, T. J., Li, J., Ackerman, S. A., and Gurka, J. J.: High-spectral- and high-temporal-resolution  
646 infrared measurements from geostationary orbit, *J. Atmos. Oceanic Technol.*, 26(11), 2273–2292,  
647 <https://doi.org/10.1175/2009JTECHA1248.1>, 2009.

648

649 Schneider, M., Ertl, B., Diekmann, C. J., Khosrawi, F., Röhling, A. N., Hase, F., Dubravica, D., García,  
650 O. E., Sepúlveda, E., Borsdorff, T., Landgraf, J., Lorente, A., Chen, H., Kivi, R., Laemmel, T., Ramonet,  
651 M., Crevoisier, C., Pernin, J., Steinbacher, M., Meinhardt, F., Deutscher, N. M., Griffith, D. W. T.,  
652 Velazco, V. A., and Pollard, D. F.: Synergetic use of IASI and TROPOMI space borne sensors for  
653 generating a tropospheric methane profile product, *Atmos. Meas. Tech. Discuss.* [preprint],  
654 <https://doi.org/10.5194/amt-2021-31>, in review, 2021.

655

656 Schwantes, K. R., Cohen, D., Mantica, P., and Glumb, R. J.: Modeling noise equivalent change in  
657 radiance (NEdN) for the Crosstrack Infrared Sounder (CrIS), *Proc. SPIE*, 4486, 456–463,  
658 <https://doi.org/10.1117/12.455128>, 2002.

659

660 Smith, N., and Barnet, C. D.: CLIMCAPS observing capability for temperature, moisture, and trace gases  
661 from AIRS/AMSU and CrIS/ATMS, *Atmos. Meas. Tech.*, 13(8), 4437–4459,  
662 <https://doi.org/10.5194/amt-13-4437-2020>, 2020.

663

664 Spurr, R., and Natraj, V.: A linearized two-stream radiative transfer code for fast approximation of  
665 multiple-scatter fields, *J. Quant. Spectrosc. Radiat. Transfer*, 112(16), 2630–2637,  
666 <https://doi.org/10.1016/j.jqsrt.2011.06.014>, 2011.

667

668 Teixeira, J., Piepmeier, J. R., Nehrir, A. R., Ao, C. O., Chen, S. S., Clayson, C. A., Fridlind, A. M.,  
669 Lebsack, M., McCarty, W., Salmun, H., Santanello, J. A., Turner, D. D., Wang, Z., and Zeng, X.: Toward  
670 a Global Planetary Boundary Layer Observing System, <https://science.nasa.gov/science-pink/s3fs-public/atoms/files/NASAPBLIncubationFinalReport.pdf>.

671

672

673 Trent, T., Boesch, H., Somkuti, P., and Scott, N. A.: Observing water vapour in the planetary boundary  
674 layer from the short-wave infrared, *Remote Sens.*, 10(9), 1469, <https://doi.org/10.3390/rs10091469>, 2018.

675 Worden, H. M., Deeter, M. N., Edwards, D. P., Gille, J. C., Drummond, J. R., and Nédélec, P. P.:  
676 Observations of near-surface carbon monoxide from space using MOPITT multispectral retrievals, J.  
677 Geophys. Res., 115(D18), D18314, <https://doi.org/10.1029/2010JD014242>, 2010.

678

679 Worden, H. M., Deeter, M. N., Frankenberg, C., George, M., Nichitiu, F., Worden, J., Aben, I., Bowman,  
680 K. W., Clerbaux, C., Coheur, P. F., de Laat, A. T. J., Detweiler, R., Drummond, J. R., Edwards, D. P.,  
681 Gille, J. C., Hurtmans, D., Luo, M., Martínez-Alonso, S., Massie, S., Pfister, G., and Warner, J. X.:  
682 Decadal record of satellite carbon monoxide observations, Atmos. Chem. Phys., 13(2), 837–850,  
683 <https://doi.org/10.5194/acp-13-837-2013>, 2013.

684

685 Worden, J. R., Turner, A. J., Bloom, A., Kulawik, S. S., Liu, J., Lee, M., Weidner, R., Bowman, K.,  
686 Frankenberg, C., Parker, R., and Payne, V. H.: Quantifying lower tropospheric methane concentrations  
687 using GOSAT near-IR and TES thermal IR measurements, Atmos. Meas. Tech., 8(8), 3433–3445,  
688 <https://doi.org/10.5194/amt-8-3433-2015>, 2015.

689

690 Xi, X., Natraj, V., Shia, R.-L., Luo, M., Zhang, Q., Newman, S., Sander, S. P., and Yung, Y. L.:  
691 Simulated retrievals for the remote sensing of CO<sub>2</sub>, CH<sub>4</sub>, CO, and H<sub>2</sub>O from geostationary orbit, Atmos.  
692 Meas. Tech., 8(11), 4817–4830, <https://doi.org/10.5194/amt-8-4817-2015>, 2015.

693

694 Yang, J., Zhang, Z., Wei, C., Lu, F., and Guo, Q.: Introducing the new generation of Chinese  
695 geostationary weather satellites, Fengyun-4, Bull. Am. Meteorol. Soc., 98(8), 1637–1658,  
696 <https://doi.org/10.1175/BAMS-D-16-0065.1>, 2017.

697

698 Yin, R., Han, W., Gao, Z., and Li, J.: Impact of high temporal resolution FY-4A Geostationary  
699 Interferometric Infrared Sounder (GIIRS) radiance measurements on typhoon forecasts: Maria (2018)  
700 case with GRAPES global 4D-Var assimilation system, Geophys. Res. Lett., 48(15), e2021GL093672,  
701 <https://doi.org/10.1029/2021GL093672>, 2021.

702

703 Yokota, T., Yoshida, Y., Eguchi, N., Ota, Y., Tanaka, T., Watanabe, H., and Maksyutov, S.: Global  
704 concentrations of CO<sub>2</sub> and CH<sub>4</sub> retrieved from GOSAT: First preliminary results, Sci. Online Lett.  
705 Atmos., 5(1), 160–163, <https://doi.org/10.2151/sola.2009-041>, 2009.

706

707 Zeng, Z.-C., Natraj, V., Xu, F., Pongetti, T. J., Shia, R.-L., Kort, E. A., Toon, G. C., Sander, S. P., and  
708 Yung, Y. L.: Constraining aerosol vertical profile in the boundary layer using hyperspectral  
709 measurements of oxygen absorption, *Geophys. Res. Lett.*, 45(19), 10772–10780,  
710 <https://doi.org/10.1029/2018gl079286>, 2018.

711

712 Zeng, Z.-C., Zhang, Q., Natraj, V., Margolis, J. S., Shia, R.-L., Newman, S., Fu, D., Pongetti, T. J., Wong,  
713 K. W., Sander, S. P., Wennberg, P. O., and Yung, Y. L.: Aerosol scattering effects on water vapor  
714 retrievals over the Los Angeles Basin, *Atmos. Chem. Phys.*, 17(4), 2495–2508,  
715 <https://doi.org/10.5194/acp-17-2495-2017>, 2017.

716

717 Zhang, Q., Natraj, V., Li, K.-F., Shia, R.-L., Fu, D., Pongetti, T. J., Sander, S. P., Roehl, C. M., and Yung,  
718 Y. L.: Accounting for aerosol scattering in the CLARS retrieval of column averaged CO<sub>2</sub> mixing ratios,  
719 *J. Geophys. Res.*, 120(14), 7205–7218, <https://doi.org/10.1002/2015jd023499>, 2015.

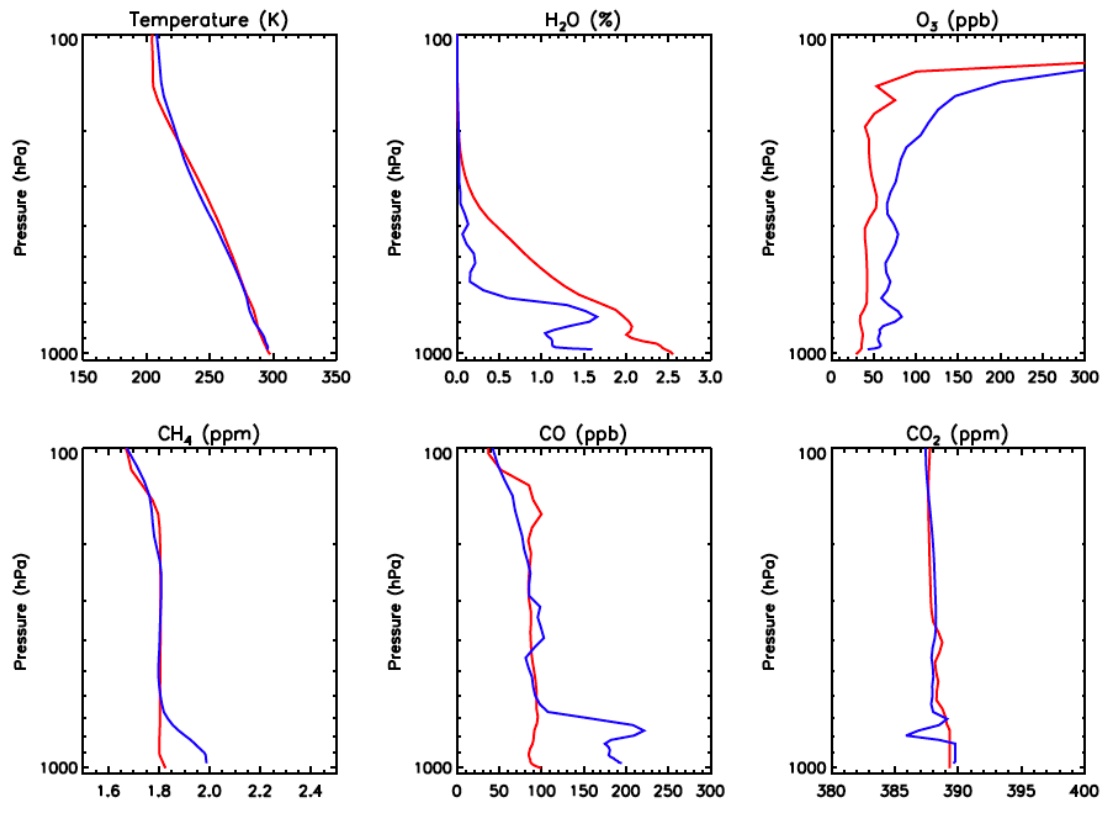
720

721 Zhang, Q., Shia, R.-L., Sander, S. P., and Yung, Y. L.: XCO<sub>2</sub> retrieval error over deserts near critical  
722 surface albedo, *Earth Space Sci.*, 3(2), 36–45, <https://doi.org/10.1002/2015ea000143>, 2016.

723

724 Zhang, Y., Jacob, D. J., Maasakkers, J. D., Sulprizio, M. P., Sheng, J.-X., Gautam, R., and Worden, J.:  
725 Monitoring global tropospheric OH concentrations using satellite observations of atmospheric methane,  
726 *Atmos. Chem. Phys.*, 18(21), 15959–15973, <https://doi.org/10.5194/acp-18-15959-2018>, 2018.

727



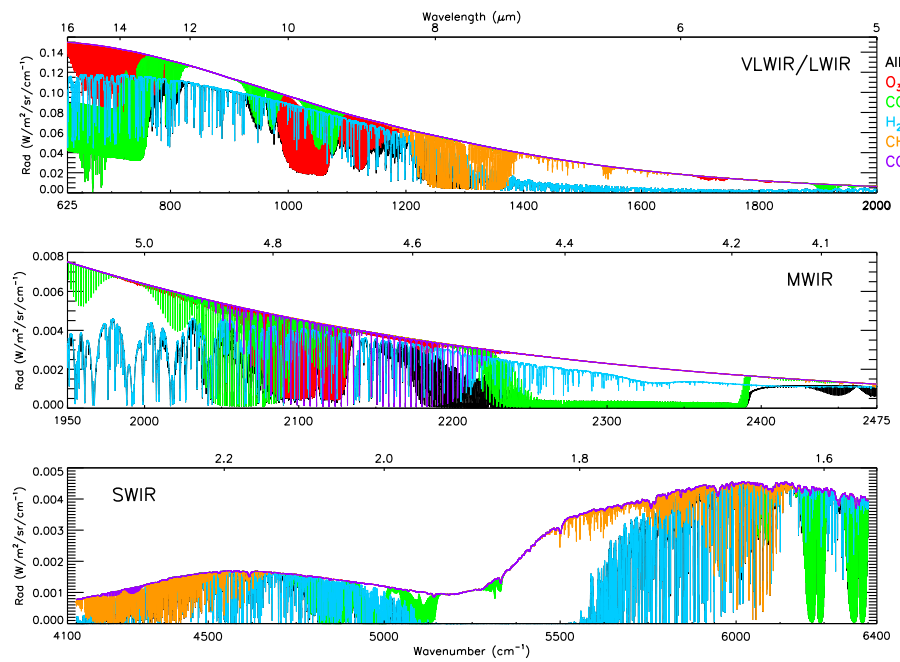
728

Houston      West Virginia

729

**Figure 1: Scenarios considered in the simulations.**

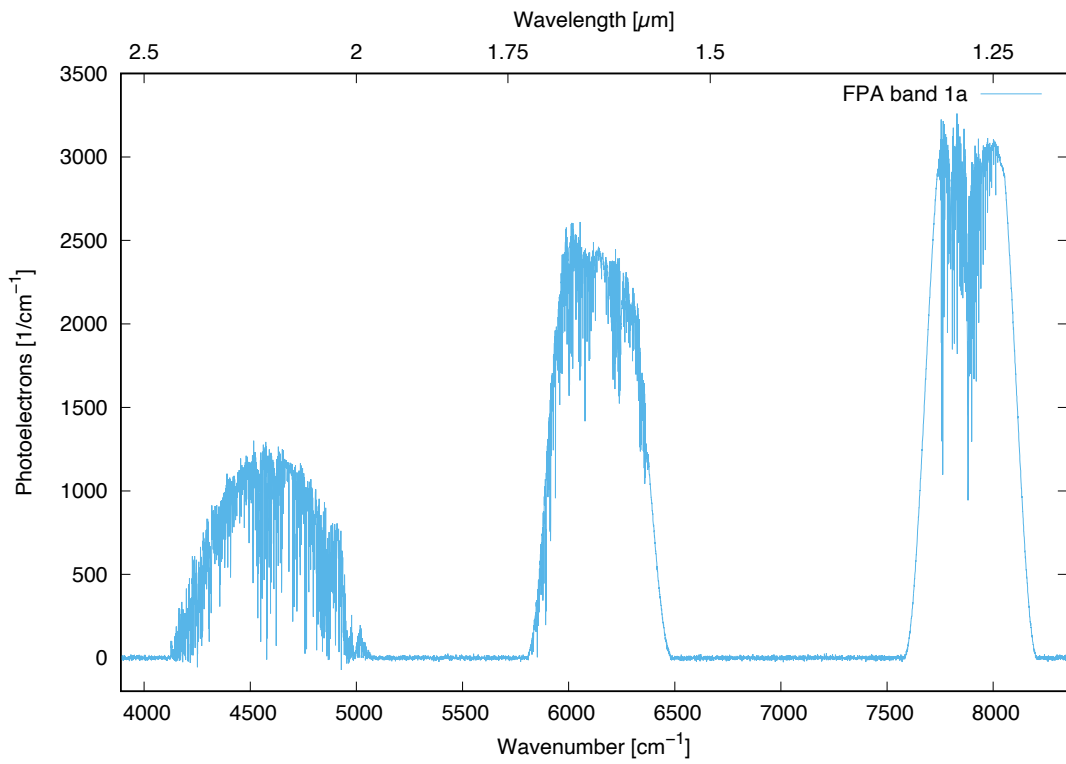
730



731

732 **Figure 2. Simulated top of the atmosphere monochromatic radiances (black) in the 650–7000 cm<sup>-1</sup> wavelength**  
 733 **range for atmospheric profile near Houston. Also shown are radiances corresponding to (red) O<sub>3</sub>, (green)**  
 734 **CO<sub>2</sub>, (blue) H<sub>2</sub>O, (orange) CH<sub>4</sub>, and (purple) CO absorption.**

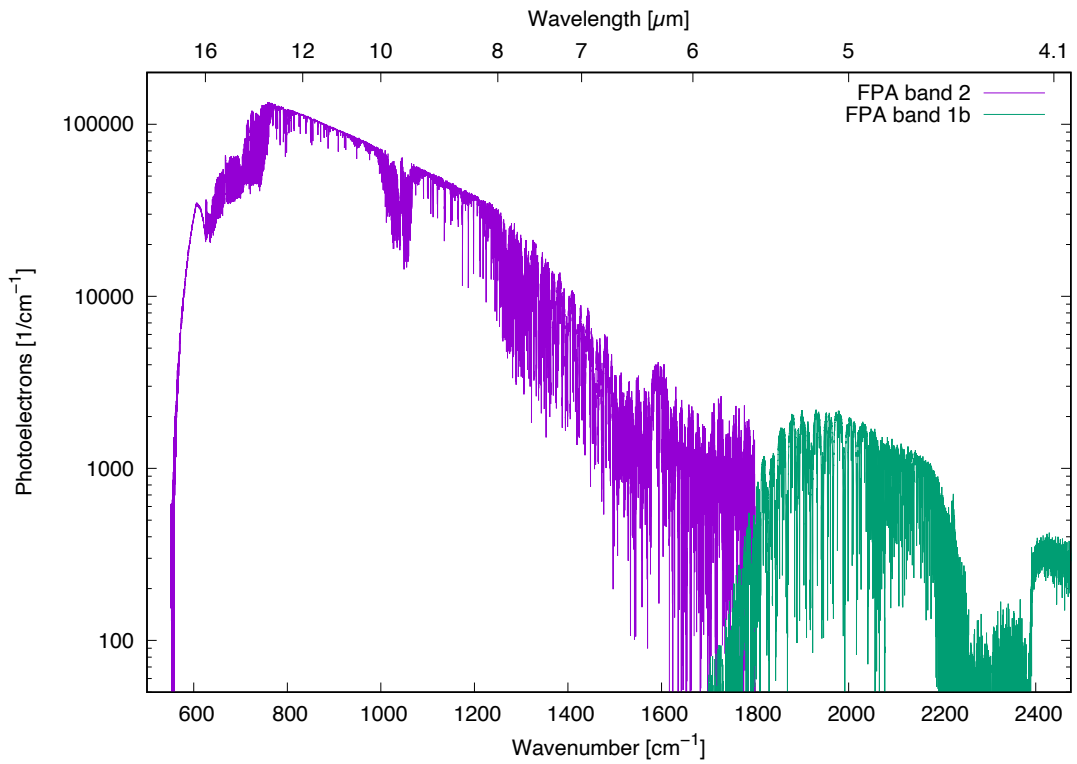
735



736

737 **Figure 3: Simulated JPL GEO-IR Sounder spectrum in the SWIR domain. The SWIR domain is sub-divided**  
 738 **into discrete bands using a triple-band interference filter to maximize the SNR in spectral regions of interest**  
 739 **(CO<sub>2</sub>, CH<sub>4</sub>, CO, H<sub>2</sub>O, and O<sub>2</sub>).**

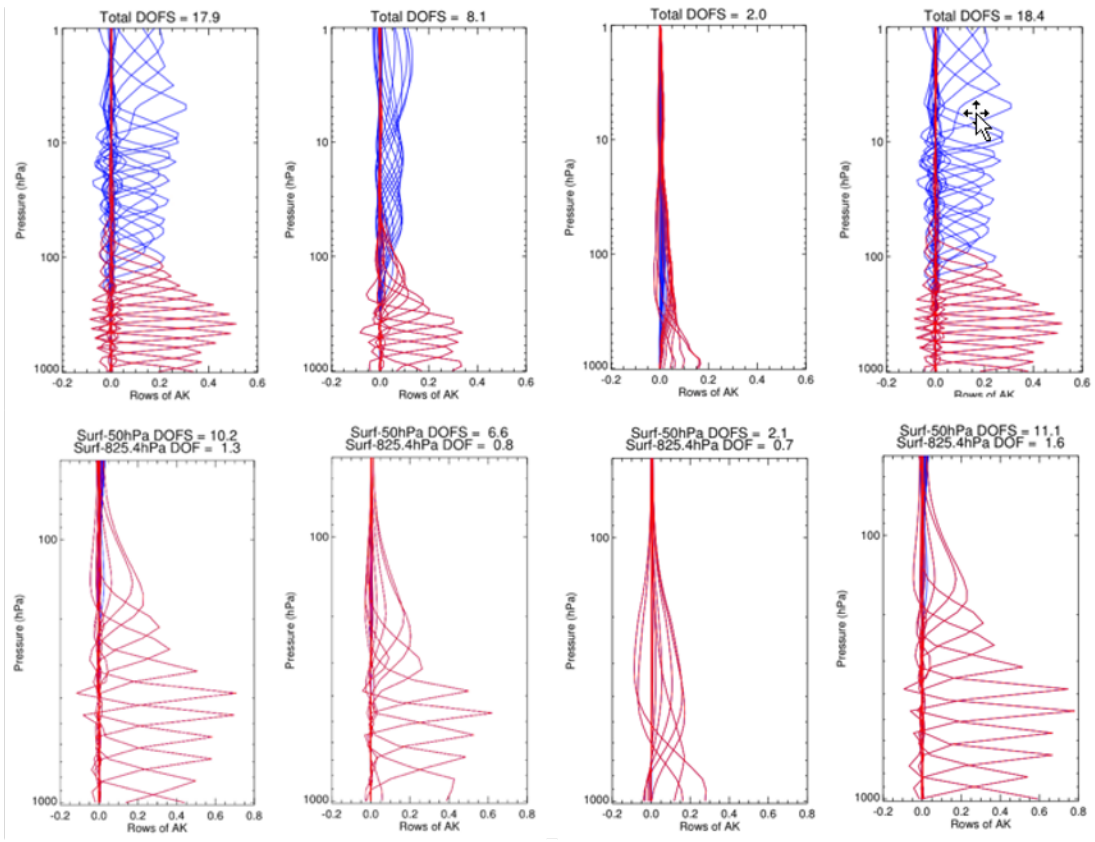
740



741

742 **Figure 4: Simulated JPL GEO-IR Sounder spectrum in the VLWIR, LWIR and MWIR domains. Note the**  
743 **logarithmic scale.**

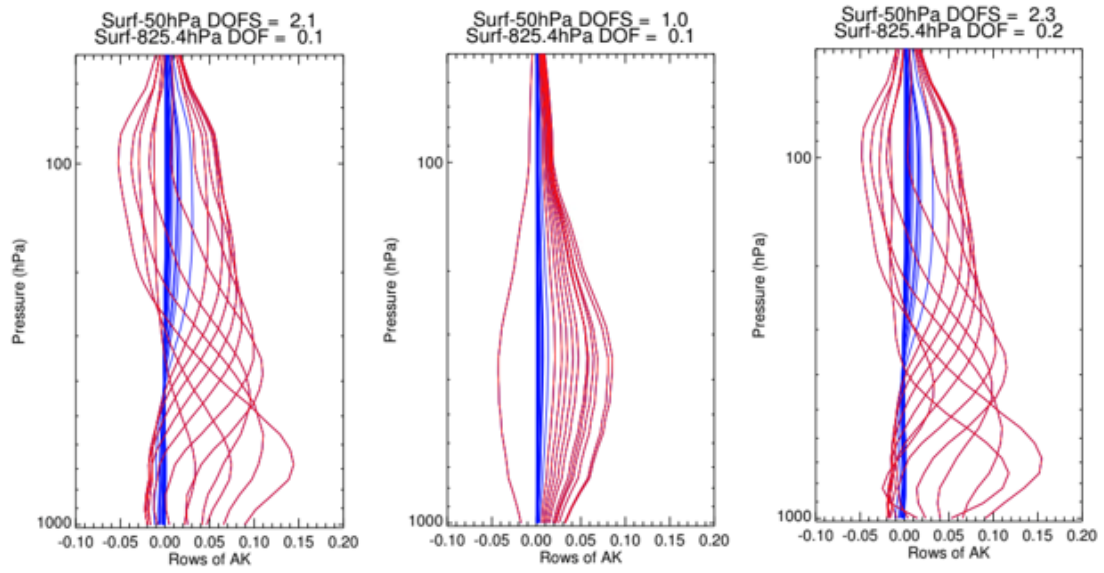
744



745

746 **Figure 5: Plots of averaging kernel rows for (top) TATM and (bottom) H<sub>2</sub>O. The spectral ranges are (from**  
 747 **left to right) VLWIR+LWIR, MWIR, SWIR, and VLWIR+LWIR+MWIR+SWIR. These results are for the**  
 748 **Houston case. The blue and red lines refer to averaging kernel rows for pressure levels above and below 100**  
 749 **hPa, respectively.**

750



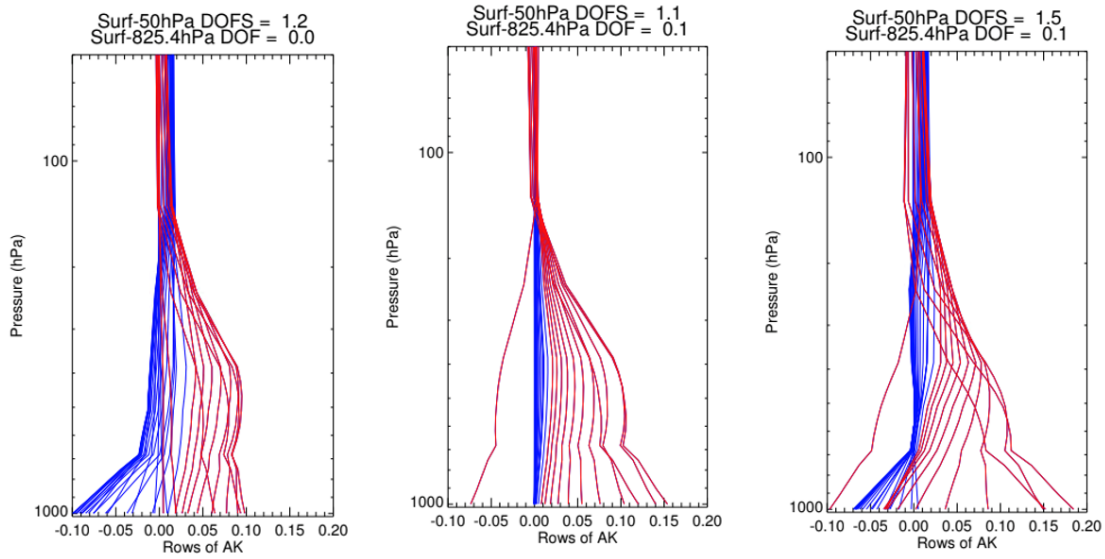
751

752 **Figure 6: Plots of averaging kernel rows for CO retrievals. The spectral ranges are (from left to right) MWIR,**

753 SWIR, and MWIR+SWIR. These results are for the West Virginia case. The color scheme is the same as in

754 Figure 5.

755



756

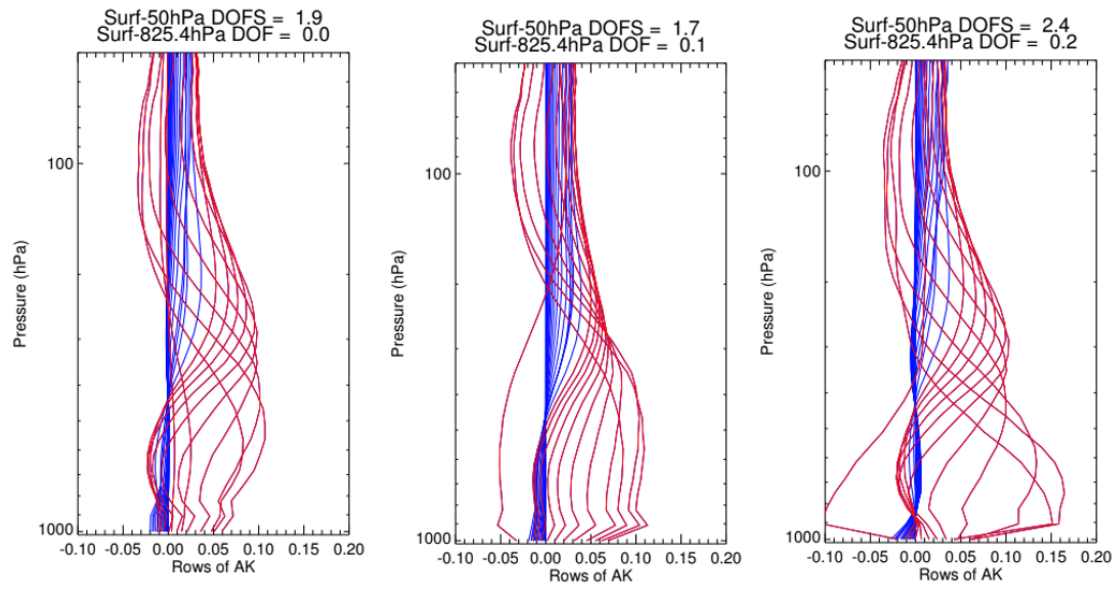
757

758

759 **Figure 7: Plots of averaging kernel rows for CO<sub>2</sub> retrievals. The spectral ranges are (from left to right)**

760 **VLWIR+MWIR, SWIR, and VLWIR+MWIR+SWIR. These results are for the West Virginia case. The color**

**scheme is the same as in Figure 5.**



761

762 **Figure 8: Plots of averaging kernel rows for CH<sub>4</sub> retrievals. The spectral ranges are (from left to right) LWIR,**

763 SWIR, and LWIR+SWIR. These results are for the West Virginia case. The color scheme is the same as in

764 Figure 5.

765

**Table 1.** Spectral ranges and their designations used in this study.

Designation	Spectral Range ( $\mu\text{m}$ )	Spectral Range ( $\text{cm}^{-1}$ )
VLWIR	>10	<1,000
LWIR	5–10	1,000–2,000
MWIR	3–5	2,000–3,333
SWIR	1–3	3,333–10,000
TIR	>3	<3,333

768 **Table 2. Current and planned missions making spaceborne, spectrally resolved measurements of TIR and**  
 769 **SWIR radiances. Note that MOPITT was designed to also offer measurements of CH<sub>4</sub>, although that did not**  
 770 **materialize (hence the gray shading).**

Orbit	Instrument/mission	T profile		H <sub>2</sub> O		CO		CH <sub>4</sub>		CO <sub>2</sub>		Winds
		TIR	TIR	TIR	SWIR	TIR	SWIR	TIR	SWIR	TIR	SWIR	
LEO	Hyperspectral TIR sounders (AIRS, CrIS, IASI, IASI-NG)	Y	Y			Y		Y		Y		
	MOPITT					Y	Y					
	GOSAT, GOSAT-2	Y	Y	Y	Y			Y	Y	Y	Y	
	OCO-2/OCO-3			Y							Y	
	TROPOMI			Y		Y		Y				
	TANSAT			Y							Y	
GEO	IRS	Y	Y			Y		Y		Y		Y
	GIIRS	Y	Y			Y		Y		Y		Y
	GeoCarb			Y			Y		Y		Y	Y
	JPL GEO-IR Sounder	Y	Y	Y	Y	Y	Y	Y	Y	Y	Y	Y

771

772

**Table 3. Spectral ranges used in this study for simulated retrievals of CO, CH<sub>4</sub> and CO<sub>2</sub>.**

Molecule	Spectral Ranges (cm <sup>-1</sup> )	Relevant For
Carbon monoxide (CO)	2000–2250 4210–4350	Air quality and carbon cycle (combustion and fire emissions)
Methane (CH <sub>4</sub> )	1210–1380 4210–4350 6000–6150	Greenhouse gas monitoring and carbon cycle (wetlands, oil and gas, agriculture)
Carbon dioxide (CO <sub>2</sub> )	650–1100 2250–2450 4810–4900 6170–6290	Greenhouse gas monitoring and carbon cycle (human emissions, status of land and ocean carbon sinks)

**Table 4. Comparison of JPL GEO-IR Sounder with other state-of-the-art instruments.**

Instrument	GIIRS	IRS	CrIS	JPL GEO-IR Sounder
Status	In space	2023 launch	In space	This study
Nationality	China	EU	US	US
Orbit	GEO	GEO	Polar	GEO
Longitude (°)	104.7 E	0–45 E	N/A	75–137 W
Spacecraft	Dedicated	Dedicated	Dedicated	Hosted payload
GSD, nadir (km)	16 (prototype) 12 (follow-ons)	4	14	4.2 (binned) 2.1 (native)
Spectral range (cm <sup>-1</sup> unless otherwise indicated)	700–1130 1650–2250 0.55–0.75 $\mu$ m	680–1210 1600–2250	650–1095 1210–1750 2155–2550	650–10,000*
Resolution (cm <sup>-1</sup> )	0.625	0.625	0.625	NSR** = 0.625, FSR = 0.1
Full Disk Revisit Time (hr)	2–3	1	12	1–2

\*FTS instrument capability

\*\* NSR = Nominal Spectral Resolution. FSR = Full Spectral Resolution. FSR mode decreases retrieval biases caused by interfering absorbers

779 **Table 5. DOFS for TATM retrievals for three spectral (MOPD) and two spatial (GSD) resolution scenarios.**

780 The values shown here are for the Houston profile.

Frequency Domain	DOFS (MOPD = 5 cm)		DOFS (MOPD = 2 cm)		DOFS (MOPD = 0.8 cm)	
	2.1 km GSD	4.2 km GSD	2.1 km GSD	4.2 km GSD	2.1 km GSD	4.2 km GSD
	VLWIR+LWIR	13.6	17.6	14.2	17.9	14.3
MWIR	5.1	7.9	5.8	8.3	6	8.1
VLWIR+LWIR+ MWIR	13.8	17.8	14.4	18.1	14.5	18.1
SWIR	0.2	1.6*	0.3	1.8*	0.4	2.0*
VLWIR+LWIR+ MWIR+SWIR	13.8	17.9*	14.6	18.3*	14.7	18.4*

781 \* Instrument noise is reduced by a factor of 5 through footprint averaging for the SWIR only,  
782 providing an effective GSD of 21 km.

783

784

**Table 6: Same as Table 5 but for H<sub>2</sub>O**

Frequency Domain	DOFS (MOPD = 5 cm)		DOFS (MOPD = 2 cm)		DOFS (MOPD = 0.8 cm)	
	2.1 km GSD	4.2 km GSD	2.1 km GSD	4.2 km GSD	2.1 km GSD	4.2 km GSD
	7.9	11.2	8.2	11.3	8.2	11.2
MWIR	4.6	6.9	5.0	7.3	4.6	6.6
VLWIR+LWIR+ MWIR	8.3	11.8	8.8	12.1	8.6	11.9
SWIR	1.2	2.2*	1.3	2.1*	1.4	2.1*
VLWIR+LWIR+ MWIR+SWIR	8.3	12.1*	8.9	12.3*	8.7	12.1*

785 \* Instrument noise is reduced by a factor of 5 through footprint averaging for the SWIR only,  
 786 providing an effective GSD of 21 km.

787

788 **Table 7. Trace gas retrieval configurations and DOFS for the West Virginia profile. TATM and H<sub>2</sub>O are**  
 789 **simultaneously retrieved when listed.**

Retrieved Species	Frequency Domain	DOFS (MOPD = 2 cm)		DOFS (MOPD = 0.8 cm)	
		2.1 km GSD	4.2 km GSD	2.1 km GSD	4.2 km GSD
O <sub>3</sub> (TATM, H <sub>2</sub> O)	LWIR	3.5	4.0	3.4	4.0
CO	MWIR	1.7	2.1	1.6	2.1
	SWIR	0.08	0.96*	0.1	0.96*
	MWIR+SWIR	1.7	2.3*	1.7	2.3*
CH <sub>4</sub> (TATM, H <sub>2</sub> O)	LWIR	1.5	2.0	1.6	2.1
	SWIR	0.7	1.9*	0.8	1.9*
	LWIR+SWIR	1.6	2.7*	1.8	2.8*
CO <sub>2</sub> (TATM, H <sub>2</sub> O)	VLWIR	1.0	1.5	1.1	1.6
	VLWIR+MWIR	1.0	1.5	1.2	1.6
	SWIR	0.3	1.1*	0.4	1.1*
	VLWIR+MWIR +SWIR	1.0	1.7*	1.2	1.9*

790 \* Instrument noise is reduced by a factor of 5 through footprint averaging for the SWIR only,  
 791 providing an effective GSD of 21 km.

792

793 **Table 8. Estimates of total and precision errors for JPL GEO-IR Sounder, CrIS and AIRS TATM and H<sub>2</sub>O**  
 794 **retrievals in the troposphere. Note that data used for CrIS and AIRS retrievals were obtained near Houston,**  
 795 **Texas in August 2020. Averaged retrieved cloud optical depths are limited to less than 0.1, consistent with**  
 796 **mostly clear-sky conditions.**

	TATM		H <sub>2</sub> O (lower-mid troposphere)	
	Total Error	Precision	Total Error	Precision
JPL GEO-IR Sounder (MWIR-only)	0.5–1.5 K	0.2–0.6 K	~8%	~5%
JPL GEO-IR Sounder (Entire spectral range)	0.3–1 K	0.1–0.3 K	~5%	~3%
CrIS	0.5–1.5 K	0.2–0.3 K	10–13%	2–3%
AIRS	0.5–1.2 K	~0.3 K	15–30%	2–5%

797